Thermal Infrared Observations of Asteroid (99942) Apophis with Herschel*

T. G. Müller[1], C. Kiss[2], P. Scheirich[3], P. Pravec[3], L. O'Rourke[4], E. Vilenius[1], and B. Altieri[4],

[1] Max-Planck-Institut für extraterrestrische Physik, Postfach 1312, Giessenbachstraße, 85741 Garching, Germany

[2] Konkoly Observatory, Research Center for Astronomy and Earth Sciences, Hungarian Academy of Sciences; Konkoly Thege 15-17, H-1121 Budapest, Hungary

[3] Astronomical Institute, Academy of Sciences of the Czech Republic, Fričova 1, CZ-25165 Ondřejov, Czech Republic

[4] European Space Astronomy Centre (ESAC), European Space Agency, Apartado de Correos 78, 28691 Villanueva de la Cañada, Madrid, Spain

Received ; accepted

ABSTRACT

The near-Earth asteroid (99942) Apophis is a potentially hazardous asteroid. We obtained far-infrared observations of this asteroid with the Herschel Space Observatory's PACS instrument at 70, 100, and 160 μm. These were taken at two epochs in January and March 2013 during a close Earth encounter. These first thermal measurements of Apophis were taken at similar phase angles before and after opposition. We performed a detailed thermophysical model analysis by using the spin and shape model recently derived from applying a 2-period Fourier series method to a large sample of well-calibrated photometric observations. We find that the tumbling asteroid Apophis has an elongated shape with a mean diameter of 375^{+14}_{-10} m (of an equal volume sphere) and a geometric V-band albedo of $0.30^{+0.05}_{-0.06}$. We find a thermal inertia in the range 250-800 $\mathrm{Jm^{-2}s^{-0.5}K^{-1}}$ (best solution at $\Gamma = 600\,\mathrm{Jm^{-2}s^{-0.5}K^{-1}}$), which can be explained by a mixture of low conductivity fine regolith with larger rocks and boulders of high thermal inertia on the surface. The thermal inertia, and other similarities with (25143) Itokawa indicate that Apophis might also have a rubble-pile structure. If we combine the new size value with the assumption of an Itokawa-like density and porosity we estimate a mass between 4.4 and 6.2 · 10^{10} kg which is more than 2-3 times larger than previous estimates. We expect that the newly derived properties will influence impact scenario studies and influence the long-term orbit predictions of Apophis.

Key words. Minor planets, asteroids: individual – Radiation mechanisms: Thermal – Techniques: photometric – Infrared: planetary systems

1. Introduction

The near-Earth asteroid 99942 Apophis was discovered in 2004 (Minor Planet Supplement 109613) and found to be on an Aten-type orbit[1] crossing the Earth's orbit in regular intervals. At that time, the object raised serious concerns following the discovery that it had a 2.7% chance of striking the planet Earth in 2029[2]. Immediate follow-up observations to address these concerns took place and provided predictions that eliminated the possibility of collision in 2029, although it does enter below the orbit of the geostationary satellites at that time. However there did remain the possibility of Apophis passing through a precise region in space (gravitational keyhole) which could set it up for an impact in the mid-term future (Farnocchia et al. 2013). Apophis remains an object with one of the highest statistical chances of impacting the Earth among all known near-Earth Asteroids.

The studies performed to determine the impact probability require a clear set of physical properties in order to understand the orbital evolution of this asteroid (Žižka & Vokrouhlický 2011; Farnocchia et al. 2013; Wlodarczyk 2013). The lack of availability of such properties (albedo, size, shape, rotation, physical structure, thermal properties) is a major limiting factor which leads to uncertainties in the role played by non-gravitational effects on that orbit. The Yarkovsky effect due to the recoil of thermally re-radiated sunlight is the most important of these non-gravitational effects.

Besides the input to the orbit evolution, the physical properties serve also to address the possible implications if an impact were to occur. A solid body of 300 m versus a rubble pile hitting the Earth implies different levels of severity as regards its ability to pass through the atmosphere unscathed to create regional versus grandscale damage.

Delbo et al. (2007a) determined from polarimetric observations an albedo of 0.33 ± 0.08 and an absolute magnitude of H = 19.7 ± 0.4 mag. These values led to a diameter of 270 ± 60 m, slightly smaller than earlier estimates in the range 320 to 970 m, depending on the assumed albedo. Binzel et al. (2009) described the results of observations they performed in the visible to near infrared (0.55 to 2.45 μm) of Apophis where they compared and modeled its reflectance spectrum with respect to the spectral and mineralogical characteristics of likely meteorite analogs. Apophis was found to be an Sq-class asteroid that most closely resembled LL ordinary chondrite meteorites in terms of spectral characteristics and interpreted olivine and pyroxene abundances. They found that composition and size similarities of Apophis with (25143) Itokawa suggested a total porosity of 40% as a current best guess for Apophis. Applying these parameters to Apophis yielded a mass estimate of $2 \cdot 10^{10}$ kg with a corresponding energy estimate of 375 Megatonnes (Mt) TNT for its potential hazard. Substantial unknowns, most notably the total porosity, allowed uncertainties in these mass and energy estimates to be as large as factors of two or three.

Up to the time of our own observations, there were no thermal infrared measurements existing on this asteroid. Observations from the Spitzer Space Telescope were not possible as Apophis was not in the Spitzer visibility region during the remainder of its mission. Due to the fact that there was no close encounter with Earth between discovery and now, there are also no groundbased N-/Q-band observations, no Akari and also no WISE observations available.

---

[*] *Herschel* is an ESA space observatory with science instruments provided by European-led Principal Investigator consortia and with important participation from NASA.

[1] The current orbit's perihelion is at 0.746 AU, aphelion at 1.0985 AU, with a=0.922 AU, i=3.33°, e=0.191.

[2] http://neo.jpl.nasa.gov/risk

http://newton.dm.unipi.it/neodys

We observed this near-Earth asteroid with the Herschel Space Observatory's (Pilbratt et al. 2010) PACS (Photodetector Array Camera and Spectrometer) instrument (Poglitsch et al. 2010) at far-infrared wavelengths (Section 2). We present our thermophysical model (TPM) analysis (Section 3) and discuss the results (Section 4).
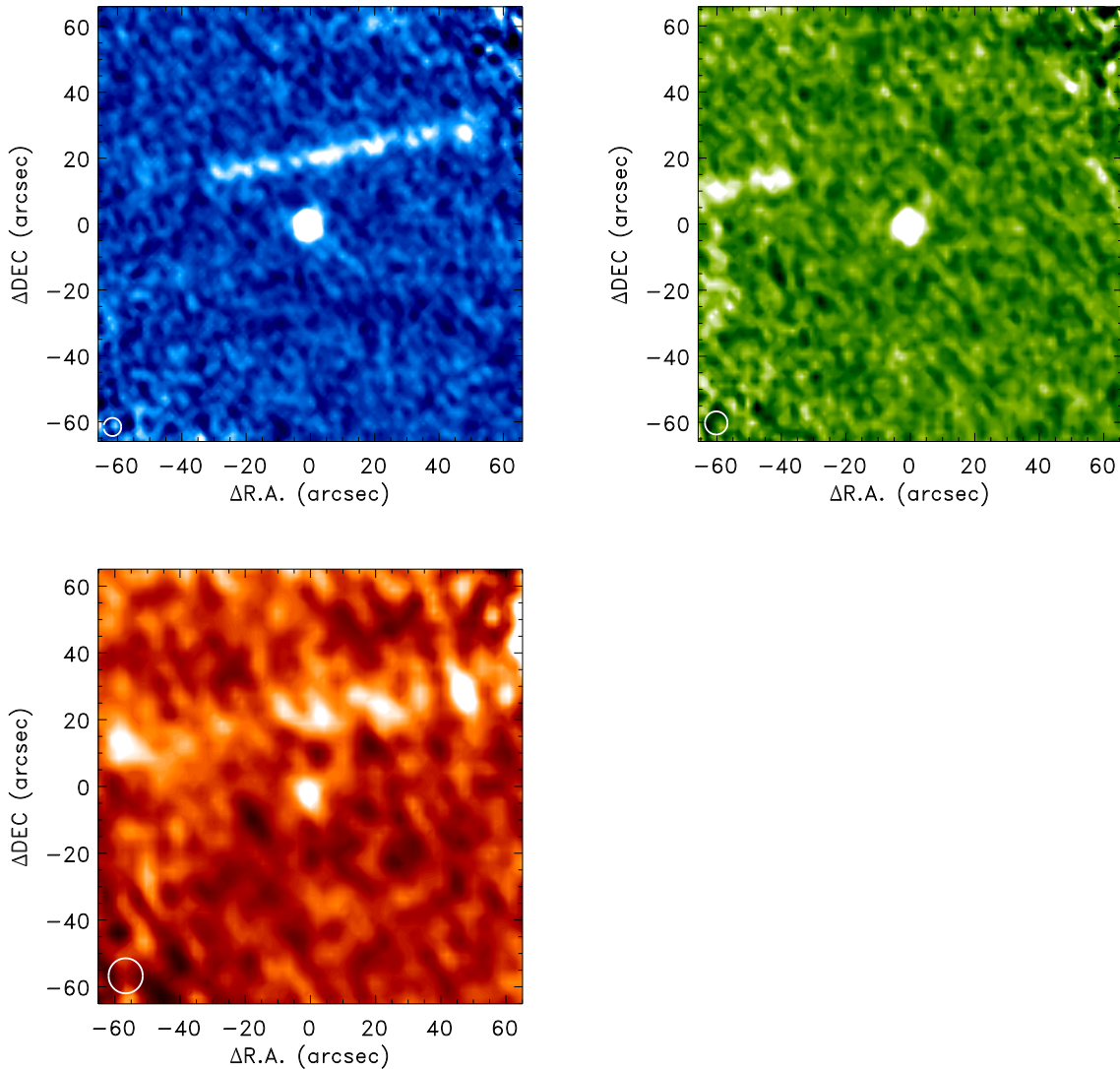
2. Far-infrared observations with Herschel-PACS

Fig. 1. The object-centered images of the target in the 3 PACS filters for the first visit on Jan. 6, 2013. Top: blue (70 μm), middle: green (100 μm), bottom: red (160 μm).

The far-infrared observations with the Herschel Space Observatory were performed in several standard PACS mini scan-map observations in tracking mode. The observations took place on Jan. 6, 2013 (four individual observations) and on Mar. 14, 2013 (one individual observation). Each individual observation consisted of several repetitions of a mini scan-map. The observational circumstances are listed in Table 1. During the first epoch all three PACS filters at 70 (blue), 100 (green), and 160 μm (red band) were used, while in the second epoch we concentrated only on the

70/160 μm filter setting due to observing time limitations. Each measurement consisted of a mini scan-map with 10 scan-legs of 3 arcmin length and separated by 4 arcsec, the scan direction was 70° (along the diagonal of the detector arrays), and the scan-speed was 20″/s. Each scan-leg is centered on the true object position at scan mid-time. The PACS photometer takes data frames with 40 Hz, but binned onboard by a factor of 4 before downlink. The total duration of our Herschel-PACS observations was about 2 h during the first epoch, split in 4 measurements of about 30 min each: 2× 6 map repetitions in the blue, 2× 7 map repetitions in the green band, each time with the red channel in parallel. During the second visit we only executed one single measurement of about 1.4 h which corresponds to 18 map repetitions in the blue/red filter setting. In this case we split the data into 6 individual datasets with 3 repetitions each.

Figure 1 shows the object-centered images of the first visit in January 2013. They are produced by stacking all frames of a given band on the source position in the first frame. The background structures in these figures are not real and related to background source artefacts caused by the re-centering of images on the rapidly changing Apophis position. During the first visit Apophis was moving in a clean part of the sky without any significant sources along the object's path. During the second visit the source moved over faint objects located in a field of diffuse background emission which we could not entirely eliminate in the reduction process. We followed the object's flux (in the background-subtracted images) and noticed a 1-2 mJy residual background emission in parts of the object's trajectory (see footnote in Table 1). In addition to the six sub-images we also combined all background-free and clean images (repetitions 4-9, 16-18) to obtain a final object-centered map for high-quality photometry.

We performed aperture photometry on the final calibrated images and estimated the flux error via photometry on artificially implemented sources in the clean vicinity around our target. The fluxes were finally corrected for colour terms due to the differences in spectral energy distribution between (99942) Apophis and the assumed constant energy spectrum νF_ν = const. in the PACS calibration scheme. The calculated colour-corrections for our best Apophis model solution are 1.005, 1.023, 1.062, at 70.0, 100.0, and 160.0 μm respectively. These values agree with the expected corrections[3] for objects with temperatures around 250 K. The absolute flux calibration error is 5% in all three bands. This error is based on the model uncertainties of the fiducial stars used in the PACS photometer flux calibration scheme (Nielbock et al. 2013; Balog et al. 2014). Since this error is identical for all our observations, we consider it at a later stage in the discussion about the quality of our derived properties. The final monochromatic flux densities and their flux errors at the PACS reference wavelengths 70.0, 100.0 and 160.0 μm are listed in Table 1.

3. Radiometric analysis

3.1. Shape and spin properties

Pravec et al. (2014) found that Apophis has a non-principal axis rotation and it is in a moderately excited Short Axis Mode state. The strongest observed lightcurve amplitude[4] is related to a retro-

---

[3] PACS technical report PICC-ME-TN-038, v1.0: `http://herschel.esac.esa.int/twiki/pub/-Public/PacsCalibrationWeb/cc_report_v1.pdf`

[4] The full (peak-to-trough) amplitude of the strongest lightcurve frequency $2P_1^{-1} = 2(P_\phi^{-1} - P_\psi^{-1})$ is 0.59 ± 0.03 mag, with the precession period P_ϕ = 27.38 ± 0.07 h and the rotation period P_ψ = 263 ± 6 h.

grade rotation with $P_1 = 30.56 \pm 0.01$ h and the angular momentum vector at $(\lambda_{ecl}, \beta_{ecl}) = (250°,$ -75°). The relevant parameters for our radiometric analysis are (i) the orientation of the object at the time of the Herschel observations, given by the object's z axis which is connected to the largest moment of inertia in the asteroid's co-rotating coordinate frame, and the angle ϕ_0 which specifies the rotation angle of the body at the given julian date. (ii) the rotation history of the object to account for thermal inertia effects (the thermal inertia is responsible for "transporting" heat to the non-illuminated parts of the surface).

Pravec et al. (2014) were also able to reconstruct the physical shape model (see Figure 3) of Apophis following the work by Kaasalainen (2001; 2001a) and Scheirich et al. (2010). The convex shape model with the non-principal axis rotation was determined by Pravec et al. to be the best-fit solution to the observed lightcurves from December 2012 to April 2013. The available photometric observations were found to cover our Herschel measurements in January 2013 very well. In March 2013 the situation is less favorable and the photometric points are sparsely distributed in the days before and after the Herschel observations (see Fig. 6 in Pravec et al. 2014).

The lightcurve-derived shape model does not have absolute size information. A dark (low albedo) and large object could explain the observed lightcurves equally well as a bright (high albedo) but much smaller object. For our analysis we used the physical shape model and the rotational properties presented in Pravec et al. (2014), the relevant coordinates and angles connected to our thermal measurements are listed in Table 2 and shown in the context of a full rotation in Figure 2.

3.2. Thermophysical model analysis

Thermophysical model (TPM) techniques are very powerful in deriving reliable sizes and albedos. In cases where enough thermal data are available and if there is already information about the object's shape and spin axis then this technique also allows to solve for thermal properties of the surface (e.g., Harris & Lagerros 2002; Müller et al. 2005). Here the radiometric analysis was done via a thermophysical model which is based on the work by Lagerros (1996; 1997; 1998). This model is frequently and successfully applied to near-Earth asteroids (e.g., Müller et al. 2004; 2005; 2011; 2012; 2013), to main-belt asteroids (e.g., Müller & Lagerros 1998; Müller & Blommaert 2004), and also to more distant objects (e.g. Horner et al. 2012; Lim et al. 2010). The TPM takes into account the true observing and illumination geometry for each observational data point, a crucial aspect for the interpretation of our Apophis observations which cover before- and after-opposition measurements[5]. The TPM allows to use any available convex shape model in combination with spin-axis properties. The heat conduction into the surface is controlled by the thermal inertia Γ, while the infrared beaming effects are calculated via a surface roughness model, implemented as concave spherical crater segments on the surface and parameterized by the root mean square (r.m.s.) slope angle. We performed our radiometric analysis with a constant emissivity of 0.9 at all wavelengths, knowing that the emissivity can decrease beyond $\sim 200\,\mu$m for some objects (e.g., Müller & Lagerros 1998; 2002), but our measurements are all at shorter wavelengths.

---

[5] Before opposition: object is leading the Sun, positive phase angle in Table 1; after opposition: object is trailing the Sun, negative phase angles

Table 1. Observing geometries (Herschel-centric) and final calibrated flux densities (FD). r_{helio} is the heliocentric distance, Δ_{obs} the object's distance from Herschel, and α is the phase-angle, with negative values after opposition. OD is Herschel's operational day, OBSID: Herschel's observation identifier. The repetitions specify the number of scan-maps performed and/or used to derived the given flux and error. The Herschel-centric apparent motions of Apophis were 205″/h (first visit in January 2013) and 58″/h (second visit in March 2013).

Julian Date mid-time	λ_{ref} [μm]	FD [mJy]	FD_{err} [mJy]	r_{helio} [AU]	Δ_{obs} [AU]	α [deg]	OD/ OBSID	repeti-tions	duration [s]
first visit[a] on Jan. 6, 2013:									
2456298.50745	70.0	36.3	1.1	1.03593	0.096247	+60.44	1333/1342258557	1- 6	1928
2456298.50745	160.0	8.7	3.3	1.03593	0.096247	+60.44	1333/1342258557	1- 6	1928
2456298.53059	100.0	22.8	1.7	1.03599	0.096234	+60.40	1333/1342258558	1- 7	2012
2456298.53059	160.0	7.4	3.8	1.03599	0.096234	+60.40	1333/1342258558	1- 7	2012
2456298.55258	70.0	37.5	1.3	1.03604	0.096221	+60.36	1333/1342258559	1- 6	1730
2456298.55258	160.0	9.8	2.5	1.03604	0.096221	+60.36	1333/1342258559	1- 6	1730
2456298.57455	100.0	25.0	1.5	1.03609	0.096208	+60.32	1333/1342258560	1- 7	2012
2456298.57455	160.0	8.2	2.2	1.03609	0.096208	+60.32	1333/1342258560	1- 7	2012
combined first visit:									
2456298.53194	70.0	36.08	0.92	1.03599	0.096233	+60.40	1342258557 + 59	all	3658
2456298.55394	100.0	22.56	1.17	1.03604	0.096220	+60.36	1342258558 + 60	all	4024
2456298.54375	160.0	9.41	1.29	1.03602	0.096226	+60.37	1342258557 ... 60	all	7682
second visit[b] on Mar. 14, 2013:									
2456365.77802	70.0	12.6[c]	2.7	1.093010	0.232276	-61.38	1400/1342267456	1- 3	828
2456365.78760	70.0	11.4	2.7	1.093003	0.232307	-61.38	1400/1342267456	4- 6	828
2456365.79719	70.0	10.4	2.7	1.092996	0.232338	-61.39	1400/1342267456	7- 9	828
2456365.80677	70.0	12.5[c]	2.6	1.092989	0.232368	-61.39	1400/1342267456	10-12	828
2456365.81635	70.0	13.3[c]	2.7	1.092983	0.232397	-61.40	1400/1342267456	13-15	828
2456365.82594	70.0	12.4	2.6	1.092976	0.232427	-61.40	1400/1342267456	16-18	828
combined second visit:									
2456365.80198	70.0	11.20	1.41	1.09299	0.232352	-61.39	1400/1342267456	selected	2484
2456365.80198	160.0	<3.2	—	1.09299	0.232352	-61.39	1400/1342267456	all	4968

Notes. [a] Light-travel time is 48.0 s; [b] light-travel time is 115.9 s; [c] Photometry is still affected by 1-2 mJy residuals from the background elimination process, not used for the final photometry on the combined measurement.

We used a mean absolute magnitude[6] of $H_V = 19.09 \pm 0.19$ mag which was derived by Pravec et al. (2014) under the assumption of a slope parameter of G=0.24 ± 0.11.

3.2.1. Initial estimate for flux change due to geometry

The average observed Apophis flux at 70 μm changed from 36.7 mJy on Jan. 6 to 11.2 mJy on Mar. 14, 2013, resulting in a flux ratio FD_{epoch1}/FD_{epoch2} of 3.2. This ratio is driven by (i) the change in

[6] The mean absolute magnitude corresponds to the mean observed cross-section.

Table 2. The Apophis orientation for the nominal rotation model during the Herschel observations. The angular velocity was 5.00 radians/day during the first visit and 5.02 radians/day during the second visit (around the true spin axis at the given times). Numbers are given in the Apophis-centric frame.

Julian Date mid-time	z-axis [deg] λ_{ecl}	β_{ecl}	rot. angle ϕ_0 [deg]	Rotation axis [deg] λ_{ecl}	β_{ecl}
first visit on Jan. 6, 2013:					
2456298.50745	19.9	-58.5	243.6	234.53	-75.51
2456298.53059	11.5	-57.5	241.2	234.39	-75.99
2456298.55258	3.7	-56.4	239.3	234.44	-76.45
2456298.57455	356.4	-55.2	237.8	234.74	-76.92
second visit on Mar. 14, 2013:					
2456365.77802	294.3	-72.9	96.2	233.35	-70.32
2456365.78760	293.1	-72.1	97.7	232.58	-70.53
2456365.79719	291.9	-71.3	99.2	231.81	-70.76
2456365.80677	290.6	-70.6	100.6	231.04	-71.01
2456365.81635	289.3	-69.8	101.9	230.38	-71.25
2456365.82594	287.9	-69.0	103.2	229.78	-71.49

observing geometry (r, Δ, α); (ii) the change in cross section due to the object's non-spherical shape and the different rotational phase; (iii) thermal effects which transport heat to non-illuminated parts of the surface.

Assuming a spherical object in instantaneous equilibrium with solar insolation (thermal inertia equals zero) would produce a very different 70 μm flux ratio FD_{epoch1}/FD_{epoch2} of 6. This calculation was the baseline for our planning of the Herschel observations in March (second epoch measurement) where we expected to see approximately 6 mJy instead of the observed 11.2 mJy. The discrepancy between expectations and observations shows that changes in the observed cross section and thermal effects, in addition to the changes in observing geometry, play a significant role and are key elements for our radiometric analysis.

3.2.2. Initial estimate for flux change due to shape effects

With the availability of Apophis' shape model and rotational properties it is also possible to calculate the influence of the apparent cross section on the observed flux. Apophis was showing a 1.21 times larger cross section during the second epoch as compared to the first epoch. The combined geometry and cross-section change would result in a 70 μm flux ratio FD_{epoch1}/FD_{epoch2} of about 3.7 which is still significantly larger than the observed ratio of 3.2. This is a strong indication that thermal effects play an important role. The effect can also nicely be seen in Figure 3: before opposition we see the object under a phase angle of about +60° with a cold morning terminator, while in the second epoch we have seen Apophis at about -61° with a warm evening side which has just rotated out of the Sun. In both cases thermal effects play a strong role: during the first epoch a

substantial part of the surface heat is transported to the non-visible side while in the second epoch the heat transport to the non-illuminated part remains visible.

3.2.3. Radiometric analysis of the first epoch data

Looking at Figure 3 (left side), we find that the observed flux from the first epoch data taken on Jan. 6, 2013 is dominated by the illuminated/heated part of the surface and the cold morning side does not contribute in a significant manner. However, depending on the thermal inertia of the top-surface layer there is some heat transported to the non-visible rear side. The conversion of the observed flux into a size and albedo solution depends therefore on the thermal inertia and larger values for the thermal inertia lead to smaller size and larger albedo estimates (see Fig. 4). We applied the radiometric method to all epoch-1 data (see first part of Table 1) simultaneously and derived the size (of an equal-volume sphere) and the geometric albedo (in V-band). For the calculations we used the true, Herschel-centric observing geometry together with the correct orientation of the object at the time of the measurements (see Table 2 and Fig. 3, left side). For signal-to-noise reasons we used the combined $100\,\mu$m flux (S/N=19.3), the combined $160\,\mu$m flux (S/N=7.3), and both individual $70\,\mu$m fluxes (S/N = 33.0 and 28.8). We find acceptable size-albedo solutions[7] for a wide range of thermal inertias and surface roughness settings. Only solutions connected to thermal inertias below ~250 Jm^{-2}s$^{-0.5}$K^{-1} can be excluded due to high χ^2-values above 1.8. Figure 4 (top) shows the derived size[8] and geometric albedo values for the full range of thermal inertias. Larger values for the thermal inertia cause more heat transport to the non-visible rear side and require therefore smaller sizes to explain the observed fluxes. For the albedo there is an opposite effect and larger thermal inertias are connected to higher albedo values. The minor influence of roughness is shown by the dashed (low r.m.s. slope angle of 0.2) and dotted-dashed (high r.m.s. slope angle of 0.9) lines. The errorbars indicate the standard deviations at each thermal inertia for the size and albedo values derived from each of the four individual flux measurements. These errorbars indicate the reproducibility of the result: the sizes and albedos connected to each of the independent measurements are inside the shown errorbars. The 5% absolute calibration error of the PACS photometery (Balog et al. 2014) is considered later in the discussion section (Section 4).

The thermal inertia changes the shape of the far-IR lightcurve considerably at the time of our observations (see Figure 5). At $70\,\mu$m (top) and at $100\,\mu$m (bottom) there is a flat part or even a secondary maximum developing for the higher thermal inertias. The low thermal inertia lightcurve shows a steady decrease in flux during the two hours of Herschel measurments. This is not seen in our time-separated observations at $70\,\mu$m and at $100\,\mu$m. The completely independent measurements in both bands seem to follow the curves for the higher thermal inertia values. At $160\,\mu$m the errorbars are too large to see a similar trend. The repeated 3-band high-SNR measurements from Jan. 6, 2013 are therefore best fit by an object with a size of 355 to 385 m (the diameter of a sphere with the volume equal to the asteroid), a geometric albedo of 0.28 to 0.33, and a thermal inertia larger than 250 Jm^{-2}s$^{-0.5}$K^{-1}.

---

[7] Good fit solutions in the sense of a weighted least-squares parameter estimation require $\chi^2_{reduced} \lesssim 1.8$ for a fit to four observational data points.

[8] The size of an equal-volume sphere.

3.2.4. Radiometric analysis of the second epoch data

Figure 3 (right side) illustrates nicely that the observed flux is influenced by the non-illuminated, but still warm part of the surface which just rotated out of the Sun. The thermal inertia influences the temperature distribution on the surface and very little heat is transported to the non-visible rear side. The conversion of the observed flux into a size and albedo solution depends therefore much less on the thermal inertia. But here we are encountering some problems: (1) The SNR of the second-epoch measurement is much lower due to the 2.4 times larger Herschel-centric distance and a significant background contamination which could not be eliminated entirely (see Table 1). (2) We only obtained a single-band detection at $70\,\mu$m and an upper limit at $160\,\mu$m, but no $100\,\mu$m point was taken. (3) The coverage in optical photometric points around epoch 2 is much poorer resulting in a less accurate model at the given orientation (see Pravec et al. 2014). The synthetic model lightcurve of the best-fit solution shows a local maximum on the decreasing branch and the reliability of the calculated cross-section is not clear.

We calculated for each thermal inertia the radiometric size and albedo solutions together with the corresponding uncertainty range. The 13% error in the observed $70\,\mu$m flux translates into a 6% error in diameter and 12% error in albedo, the $160\,\mu$m detection limit unfortunately does not constrain the solution in a noticable way. As a consequence, the full range of thermal inertias is compatible with our epoch 2 data. The corresponding size and albedo values range from $370\,$m to $430\,$m and from 0.30 to 0.22, respectively.

3.2.5. Radiometric analysis of the combined data set

As a final step, we combined the radiometric results of Sections 3.2.3 and 3.2.4 while considering the derived errors. We calculated for each thermal inertia the weighted mean size and albedo solution and used our TPM setup (considering also the changing orientation state of the object) to make flux predictions for the four epoch-1 and one epoch-2 data points. Figure 6 shows the reduced χ^2 values together with the 1-σ confidence level for five independent measurements which is around 1.7. The three different levels of surface roughness are shown as dashed line ($\rho = 0.2$, low roughness), solid line ($\rho = 0.5$, intermediate roughness), and dashed-dotted line ($\rho = 0.9$, very high roughness). The best solution is found at thermal inertia values around $600\,\mathrm{Jm^{-2}s^{-0.5}K^{-1}}$, which is about mid-way inside the $\sim$100-1500$\,\mathrm{Jm^{-2}s^{-0.5}K^{-1}}$ formal acceptance range. The connected size and albedo values are 368-374$\,$m and 0.30-0.31, respectively, with this solution being dominated by the high-quality epoch-1 data. Giving a stronger weight to the epoch-2 observations shifts the χ^2-minima to lower thermal inertias: if we weight the epoch-1 and epoch-2 solutions simply by the number of independent measurements (here 4:1) then we find the χ^2-minima at a thermal inertia of around 300-350$\,\mathrm{Jm^{-2}s^{-0.5}K^{-1}}$ and values above 800$\,\mathrm{Jm^{-2}s^{-0.5}K^{-1}}$ would be excluded. The corresponding sizes are about 10$\,$m larger and the albedo is around 0.29, but the overall match to the observations is degraded with reduced χ^2 values just below 1.7. This kind of "weighting by number of observations" is somewhat arbitrary, but it shows how a better balanced (higher S/N) second epoch measurement could have influenced our results. In Section 4 we continue with the correct weighting of the observations taking into account the observational errorbars.

4. Discussions

The radiometric method has been found to work reliably for objects where shape and spin properties are known (e.g., O'Rourke et al. 2012 or Müller et al. 2014). The application to tumbling objects is more complex and requires the knowledge of the object's orientation and its spin axis at the times of the thermal measurements. For our epoch-1 data set, the tumbling is not critical since the observed flux is clearly dominated by the illuminated part of the surface. The observed flux is not influenced by the path of the heat transport to the non-visible rear side, independent whether the object rotates around the moment of inertia or the true spin axis. For our epoch-2 data, the situation is slightly different since the temperature distribution on the warm evening side contributes to the observed disk-integrated flux. In this case the tumbling causes a slight spatial displacement of the contributing warm region close to the terminator. It may be that our epoch-2 flux is slightly influenced by this effect and that our model predictions are therefore too low. A careful investigation showed us that the temperature of a very small region close to the rim and outside the direct sun illumination might in reality be higher than in our TPM calculations. But the impact on the disk-integrated flux is well below 5% and the consequences for our radiometric results are negligible. The error bars in the epoch-2 observation are simply too large.

The final uncertainties of the derived size and albedo solutions depend mainly on the quality of the thermal measurements. A 10% flux error translates typically in a 5% error in equivalent size and about 10% in geometric albedo. With several independent measurements the errors can reduce to even smaller values. But this is only the case when the H-magnitude is precisely known and the thermal inertia is well constrained by the available observational dataset. Our dataset has a good coverage in thermal wavelengths, as well as phase angles before and after opposition which is sufficient to determine the thermal inertia reliably. However, due to the above mentioned problems with epoch 2 the situation is not perfect. The epoch-1 data indicate thermal inertias larger than about $250\,\mathrm{Jm^{-2}s^{-0.5}K^{-1}}$, while the combined data set excludes only the largest values above about $1500\,\mathrm{Jm^{-2}s^{-0.5}K^{-1}}$. Delbo et al. (2007b) found an average thermal inertia of $200 \pm 40\,\mathrm{Jm^{-2}s^{-0.5}K^{-1}}$ for a sample of km-sized near-Earth objects with a maximum derived value of $750\,\mathrm{Jm^{-2}s^{-0.5}K^{-1}}$. We investigated the effects of very high thermal inertia values above $800\,\mathrm{Jm^{-2}s^{-0.5}K^{-1}}$ in the context of phase-angle and wavelength trends (as shown in Fig. 7). Although statistically still possible, these high values produce a trend in the observation-to-model ratios with phase angle and cause also a poor match to our most reliable $70\,\mu$m fluxes. The most likely range for the thermal inertia is therefore 250-$800\,\mathrm{Jm^{-2}s^{-0.5}K^{-1}}$, with our best solution connected to $600\,\mathrm{Jm^{-2}s^{-0.5}K^{-1}}$. These high values for the thermal inertia can be explained by a mixture of (very little) low conductivity fine regolith with larger rocks and boulders of high thermal inertia on the surface (see also discussions in Müller et al. 2012, 2013, 2014). If we take our best solution for the thermal inertia and assume a surface density of lunar regolith ($1.4\,\mathrm{g\,cm^{-3}}$), and that the heat capacity is somewhere between lunar regolith ($640\,\mathrm{J\,kg^{-1}K^{-1}}$) and granite ($890\,\mathrm{J\,kg^{-1}K^{-1}}$) then the thermal conductivity κ would be 0.3-$0.4\,\mathrm{W\,K^{-1}m^{-1}}$. This is compatible with Itokawa's $0.3\,\mathrm{W\,K^{-1}m^{-1}}$ (Müller et al. 2005) whereas the typical value for near-Earth asteroids is $0.08\,\mathrm{W\,K^{-1}m^{-1}}$ (Mueller M. 2007). If we take the full range of uncertainties into account ($\Gamma = 250$-$800\,\mathrm{Jm^{-2}s^{-0.5}K^{-1}}$, heat capacity 450-$1200\,\mathrm{J\,kg^{-1}K^{-1}}$, and surface density 1.3-$2.0\,\mathrm{g\,cm^{-3}}$) then the range for thermal conductivity would be 0.03-$1.1\,\mathrm{W\,K^{-1}m^{-1}}$, which is a range of two orders of magnitude.

The size range corresponding to our thermal inertia solution is 371 to 385 m (best solution 375 m) with a statistical error of about 6 m only. The smallest radiometric size solutions are produced by the high-roughness and high-inertia settings in the TPM, while the largest sizes are related to low-roughness/low-inertia settings (see also Rozitis & Green 2011 for a discussion on the degeneracy between roughness and thermal inertia). Since the PACS photometric system is only accurate on a 5% level (Balog et al. 2014), we have to consider it also in the context of our size solution[9]. The final size value is therefore 375^{+14}_{-10} m.

Our derived albedo range of 0.28 to 0.31 (larger values for high-roughness, high-inertia case) has a very small statistical error below 3%. But here we have to include the influence of the absolute flux calibration (5%), as well as the H-magnitude error of ± 0.19 mag which is the dominating factor for the final solution. Overall, we find a geometric albedo solution of $0.30^{+0.05}_{-0.06}$. This value is in nice agreement with the Delbo et al. (2007a) of 0.33 ± 0.08, derived from polarimetric observations. The small size solution of 270 ± 60 m by Delbo et al. (2007a) was mainly related to their H-magnitude which is very different from the value by Pravec et al. (2014) which we used here. We can now also determine the bolometric Bond albedo A. The uncertainty in G translates into an uncertainty in the phase integral q (Bowell et al. 1989), combined with a 5% accuracy of the q-G relation (Muinonen et al. 2010), we obtain a Bond albedo of $A = q \cdot p_V = 0.14^{+0.03}_{-0.04}$.

Figures 7 and 8 show our best model solution at intermediate roughness level in different representations. In Figure 7 we present the observations divided by the corresponding model solutions as a function of phase angle (top) and as a function of wavelength (bottom). No trends with phase angle or wavelength can be seen. Figure 8 shows the observations and the model solution on an absolute scale. Here we also show the $160\,\mu$m upper limit from epoch 2 which is in nice agreement with the model solution.

Binzel et al. (2009) found compositional similarities between 99942 Apophis and 25143 Itokawa. They both are in a similar size range, have similar albedos and similar thermal inertias. The measured density of Itokawa is 1.9 ± 0.13 g/cm^3 (Fujiwara et al. 2006; Abe et al. 2006 found a slightly higher density of 1.95 ± 0.14 g/cm^3). Using Itokawa's density and our new size estimate gives a mass estimate of $5.2^{+0.7}_{-0.6} \cdot 10^{10}$ kg. Both Itokawa and Apophis have been interpreted to be analoguous to LL chondrite meteorites (Fujiwara et al. 2006; Binzel et al. 2009). The bulk density of meteorites of that type is 3.21 ± 0.22 g/cm^3 (Britt & Consolmagno 2003). A larger uncertainty is in the macro-porosity of Apophis. Britt et al. (2002) report that asteroids' macro-porosities may be up to 50%. The porosity of Itokawa is 41% (Abe et al. 2006). Assuming a porosity range of 30-50% for Apophis implies a mass between 4.4 and $6.2 \cdot 10^{10}$ kg.

The comparison with Itokawa is interesting in many aspects: The rubble-pile near-Earth asteroid 25143 Itokawa has an effective size of 327.5 ± 5.5 m (Fujiwara et al. 2006), just 13% smaller than Apophis. Both objects have almost identical geometric albedos: 0.29 ± 0.02 for Itokawa (Bernardi et al. 2009) compared to $0.30^{+0.05}_{-0.06}$ for Apophis. Also the thermal inertias compare very well: Müller et al. (2014) found 700 ± 200 Jm^{-2}s$^{-0.5}$K^{-1} for Itokawa, well within the derived range for Apophis. Itokawa has a SIV-type taxonomic classification (Binzel et al. 2001) and the Hayabusa data revealed an olivine-rich mineral assemblage silimar to LL5 or LL6 chondrites (Abe et al. 2006; Okada et al. 2006). Apophis is characterised as an Sq-type that most closely resembles LL ordinary

---

[9] We added quadratically the statistical size error with a 2.5% size error related to the 5% in absolute flux calibration.

chondrite meteorites (Binzel et al. 2009). The high thermal inertia indicates a lack (or only very small amounts) of low-conductivity fine regolith on the surface. The formation of a thick regolith (typically with Γ-values below $100\,\mathrm{Jm^{-2}s^{-0.5}K^{-1}}$) might have been hampered by frequent seismic influences. Such processes can reorganise the body's interior and surface over short time scales if the object has a rubble-pile structure. Apophis is also in the size range predominated by asteroids with cohesionless structures (Pravec et al. 2007). On the other hand, the density of S-type asteroids is distributed in a very narrow density interval, slightly below the density of their associated meteorites, the ordinary chondrites (Carry 2012). The macroporosity for this type of asteroids is generally smaller than 30% and pointing to coherent interiors, with cracks and fractures, but not rubble piles. Interestingly, the four S-type asteroids listed by Carry (2012) with sizes below a few kilometres and with high quality density information (quality codes A, B, or C) all have densities below $2\,\mathrm{g\,cm^{-3}}$ and a porosity of 40% or above, indicative of a rubble-pile structure. Overall, Apophis' size, the surface characteristics related to a relatively high thermal inertia, and the comparison with similar-size objects, make a cohesionless structure more likely.

The newly derived properties will influence the long-term orbit predictions. Chesley et al. (2003; 2008) and Vokrouhlický et al. (2008) found that the Yarkovsky effect which is due to the recoil of thermally re-radiated sunlight is acting on many near-Earth asteroids. It is the most significant non-gravitational force to be considered for risk analysis studies (e.g., Giorgini et al. 2002, 2008; Chesley 2006). The calculation of the Yarkovsky orbit drift requires -in addition to the spin state which was determined by Pravec et al. (2014)- also some knowledge about the object's size, bulk density, and surface thermal inertia. Our work will contribute with information about size and thermal inertia (Vokrouhlický et al., in preparation). The bulk density can be estimated from the Yarkovsky-related orbit change, expected to be detected by radar observations during the next close Earth approach in September 2021 (Farnocchia et al. 2013). Žižka & Vokrouhlický (2011) showed that also the solar radiation pressure has a small, but relevant effect on Apophis' orbit which might be noticable after the very close Earth encounter in 2029. Here it is mainly the size and bulk density which play a role. The combined non-gravitational forces -Yarkovsky effect and solar radiation pressure- cause small orbit drifts up to a few kilometers per decade in case of Apophis (Farnocchia et al. 2013). In comparison, the extension of the keyholes associated with Earth-impacts after the 2029 close encounter are in the order of a 100 m or smaller. The studies of the non-gravitational orbit perturbations are therefore important to estimate the distance between the true trajectory and the locations of the dangerous keyholes.

5. Conclusions

The shape and spin properties of Apophis presented by Pravec et al. (2014) were the key elements for our radiometric analysis. The interpretation of the ~3.5 h of Herschel-PACS measurements in January and March 2013 was done using a well-tested and validated thermophysical model. Applying the radiometric method to a tumbling object is more complex, but it works reliably if the object's orientation and its spin axis is known at the epochs of the thermal measurements. We found the following results:

1. The radiometric size solution is $\mathrm{D}_{eff} = 375^{+14}_{-10}\,\mathrm{m}$; this is the scaling factor for the shape model presented in Pravec et al. (2014) and corresponds to the size of an equal volume sphere.

2. The geometric V-band albedo was found to be $p_V = 0.30^{+0.05}_{-0.06}$, almost identical to the value found for the Hayabusa rendezvous target 25143 Itokawa; the corresponding bolometric Bond albedo A is $0.14^{+0.03}_{-0.04}$.

3. A thermal inertia of $\Gamma = 600^{+200}_{-350} \, Jm^{-2}s^{-0.5}K^{-1}$ explains best our combined dataset comprising three different bands and two different epochs.

4. Using either Itokawa's bulk density information or a rock density of $3.2 \, g/cm^3$ combined with 30-50% porosity, we calculate a mass of $(5.3 \pm 0.9) \cdot 10^{10} \, kg$ which is 2 to 3 times higher than earlier estimates.

5. No information about surface roughness can be derived from the radiometric analysis of our measurements due to the lack of observations at shorter wavelengths and smaller phase angles close to opposition. But Apophis' thermal inertia is similar to the value derived for Itokawa and this might point to a surface of comparable roughness.

6. Apophis' size, the surface characteristics related to the high thermal inertia, and the comparison with similar-size objects, make a cohesionless structure more likely.

The interior structure -rubble pile or coherent body- is relevant in the context of impact scenario studies. In case of a rubble-pile structure (which is the more likely option) pre-collision encounters with planets could disrupt the body by tidal forces while a more solid interior would leave the object intact. We also expect that the newly derived properties will affect the long-term orbit predictions of Apophis which is influenced by the Yarkovsky effect and in second order also by the solar radiation pressure. In this context, the radiometrically derived size and thermal inertia will play a significant role in risk-analysis studies beyond Apophis' close encounter with Earth in 2029.

References

Abe, S., Mukai, T., Hirata, N. et al. 2006, Science, 312, 1344-1347

Balog, Z., Müller, T. G., Nielbock, M. et al. 2014, Experimental Astronomy, accepted, DOI: 10.1007/s10686-013-9352-3

Bernardi, F., Micheli, M. & Tholen, D. J. 2009, Meteorit. Planet. Sci., 44, 1849

Binzel, R. P., Rivkin, A. S., Bus, S. J., et al. 2001, Meteorit. Planet. Sci. (Suppl.), 36, A20

Binzel, R. P., Rivkin, A. S., Thomas, C. A. et al. 2009, Icarus 200, 480-485

Bowell, E., Hapke, B., Domingue, D. et al. 1989, in Asteroids II, R.P. Binzel, T. Gehrels, M. Shapley Matthews (Eds.), Univ. of Arizona Press, 524-556

Britt, D. T., Yeomans, D., Housen, K., Consolmagno, G. 2002, in Asteroids III, W. F. Bottke Jr., A. Cellino, P. Paolicchi, and R. P. Binzel (eds), University of Arizona Press, Tucson, p.485-500

Britt, D. T. & Consolmagno, G. 2003, M&PS, 38, 1161

Carry, B. 2012, P&SS 73, 98-118

Chesley, S. R., Ostro, S. J., Vokrouhlický, D. et al. 2003, Science 302, 1739-1742

Chesley, S. R. 2006, in: Lazzaro, D., Ferraz-Mello, S., Fernández, J. (Eds), Asteroids, Comets, Meteors, Cambridge University Press, Cambridge, 215-228

Chesley, S. R., Vokrouhlický, D., Ostro, S. J. et al. 2008, Asteroids, Comets, Meteors 2008, Baltimore, Maryland, Contribution No. 1405, Paper Id. 8330

Delbo, M., Cellino, A., Tedesco, E. F. 2007, Icarus 188, 266-269

Delbo, M., dell'Oro, A., Harris, A. W. et al. 2007, Icarus, 190, 236

Farnocchia, D., Chesley, S. R., Chodas, P. W. et al. 2013, Icarus 224, 192-200

Fujiwara, A., Kawaguchi, J., Uesugi, K. et al. 2006, Science, 312, 1330

Giorgini, J. D., ... 2002, Science 296, 132-136

Giorgini, J. D., Benner, L. A. M., Ostro, S. J. et al. 2008, Icarus 193, 1-19

Harris, A. W. & Lagerros, J. S. V. 2002, in Asteroids III, W. F. Bottke Jr., A. Cellino, P. Paolicchi, and R. P. Binzel (eds),
     University of Arizona Press, Tucson, p.205-218

Horner, J., Müller, T. G., Lykawka, P. S. 2012, MNRAS 423, 2587-2596

Kaasalainen, M. & Torppa, J. 2001, Icarus, 153, 24

Kaasalainen, M., Torppa, J. & Muinonen, K. 2001, Icarus, 153, 37

Lagerros, J. S. V. 1996, A&A 310, 1011

Lagerros, J. S. V. 1997, A&A 325, 1226

Lagerros, J. S. V. 1998, A&A 332, 1123

Lim, T. L., Stansberry, J., Müller, T. G. et al. 2010, A&A 518, 148-152

Müller, T. G. & Lagerros, J. S. V. 1998, A&A, 338, 340-352

Müller, T. G. & Lagerros, J. S. V. 1998, A&A, 381, 324-339

Müller, T. G. & Blommaert, J. A. D. L. 2004, A&A, 418, 347-356

Müller, T. G., Sterzik, M. F., Schütz, O. et al. 2004, A&A, 424, 1075-1080

Mueller, M. 2007, PhD thesis, Freie Universität Berlin, Germany, http://www.diss.fu-berlin.de/diss/receive/FUDISS_thesis_000000002596

Müller, T. G., Sekiguchi, T., Kaasalainen, M. et al. 2005, A&A, 443, 347-355

Müller, T. G., Ďurech, J., Hasegawa, S. et al. 2011, A&A, 525, 145

Müller, T. G., O'Rourke, L., Barucci, A. M. et al. 2012, A&A, 548, 36-45

Müller, T. G., Miyata, T., Kiss, C. et al. 2013, A&A, 558, 97

Müller, T. G., Hasegawa, S. & Usui, F. 2014, PASJ, accepted

Muinonen, K., Belskaya, I. N., Cellino, A. et al. 2010, Icarus 209, 542

Nielbock, M., Müller, T. G., Balog, Z. et al. 2013, Experimental Astronomy, 36, 631

Okada, T., Shirai, K., Yamamoto, Y., et al. 2006, Science, 312, 1338

O'Rourke, L., Müller, T., Valtchanov, I., et al. 2012, Planet. Space Sci., 66, 192

Pilbratt, G.L., Riedinger, J.R., Passvogel, T. et al. 2010, A&A, 518, L1

Poglitsch, A., Waelkens, C., Geis, N. et al. 2010, A&A, 518, L2

Pravec, P., Harris, A. W., Warner, B. D. 2007, in: Milani, A., Valsecchi, G. B., Vokrouhlický, D. (Eds.), Proc. IAU Symp,
     vol. 236. Cambridge Univ. Press, Cambridge, 167-176

Pravec, P., Scheirich, P., Ďurech, J. et al. 2014, Icarus, in press

Rozitis, B. & Green, S. F. 2011, MNRAS, 415, 2042

Scheirich, P., Durech, J., Pravec, P. et al. 2010, M&PS, 45, 1804

Vokrouhlický, D., Chesley, S. R., Matson, R. D. 2008, AJ 135, 2336-2340

Vokrouhlický, D. et al., in preparation

Wlodarczyk, I. 2013, MNRAS, 434, 3055-3060

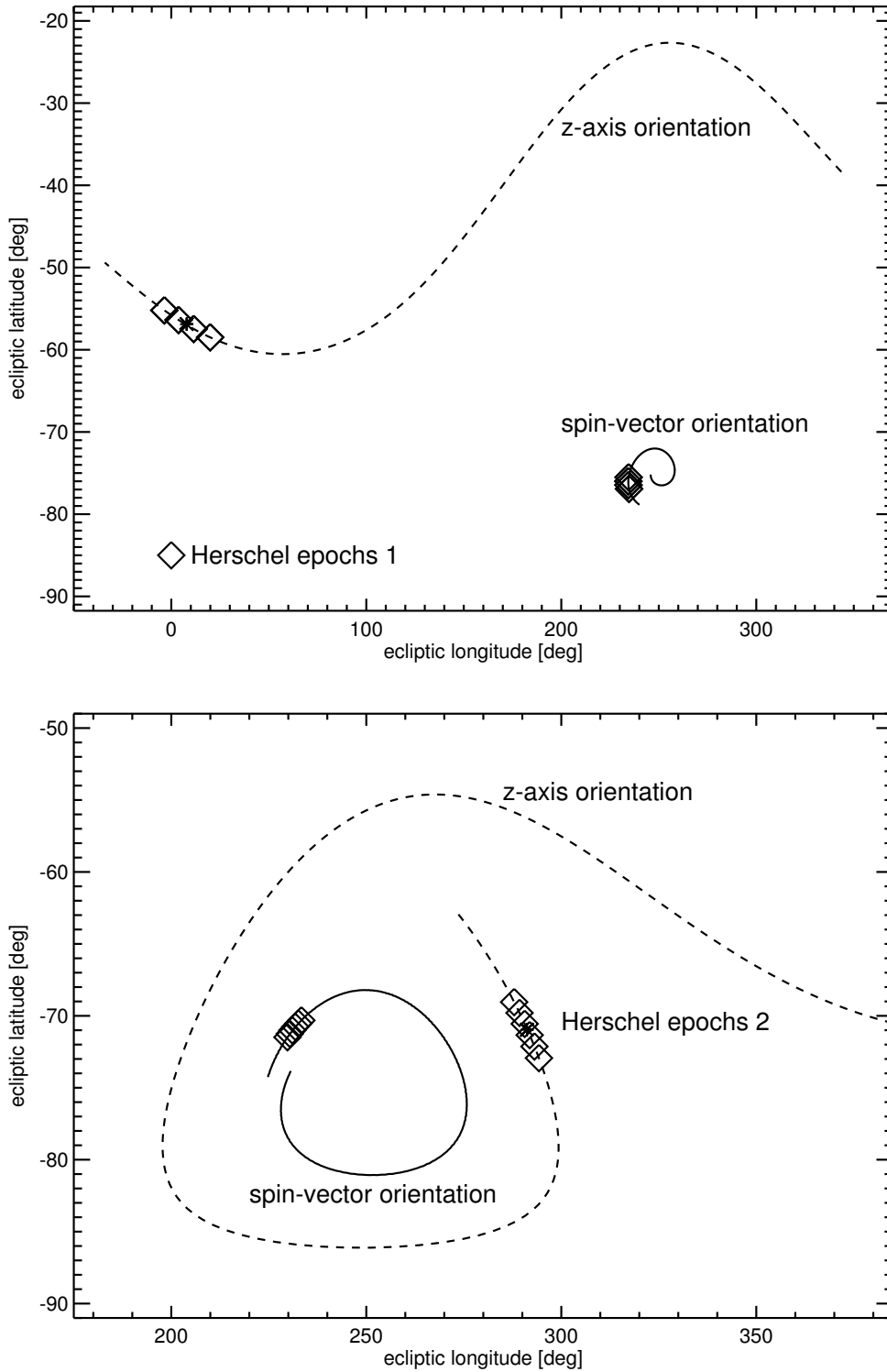Žižka, J. & Vokrouhlický, D. 2011, Icarus, 211, 511-518

Fig. 2. Variations of the object's z-axis and spin-vector orientation during a full rotation of 30.56 h, starting about 26 h before the first Herschel measurement and ending about 2 h after the last measurement. The epochs of the Herschel observations (from Table 1) are shown as diamonds. The z axis (dashed line) is connected to the largest moment of inertia in the asteroid's co-rotating coordinate frame, the solid line shows how the orientation of the object's spin axis changes with time. Top: covering the first observations on Jan. 6, 2013; bottom: covering the second observation on Mar. 14, 2013.
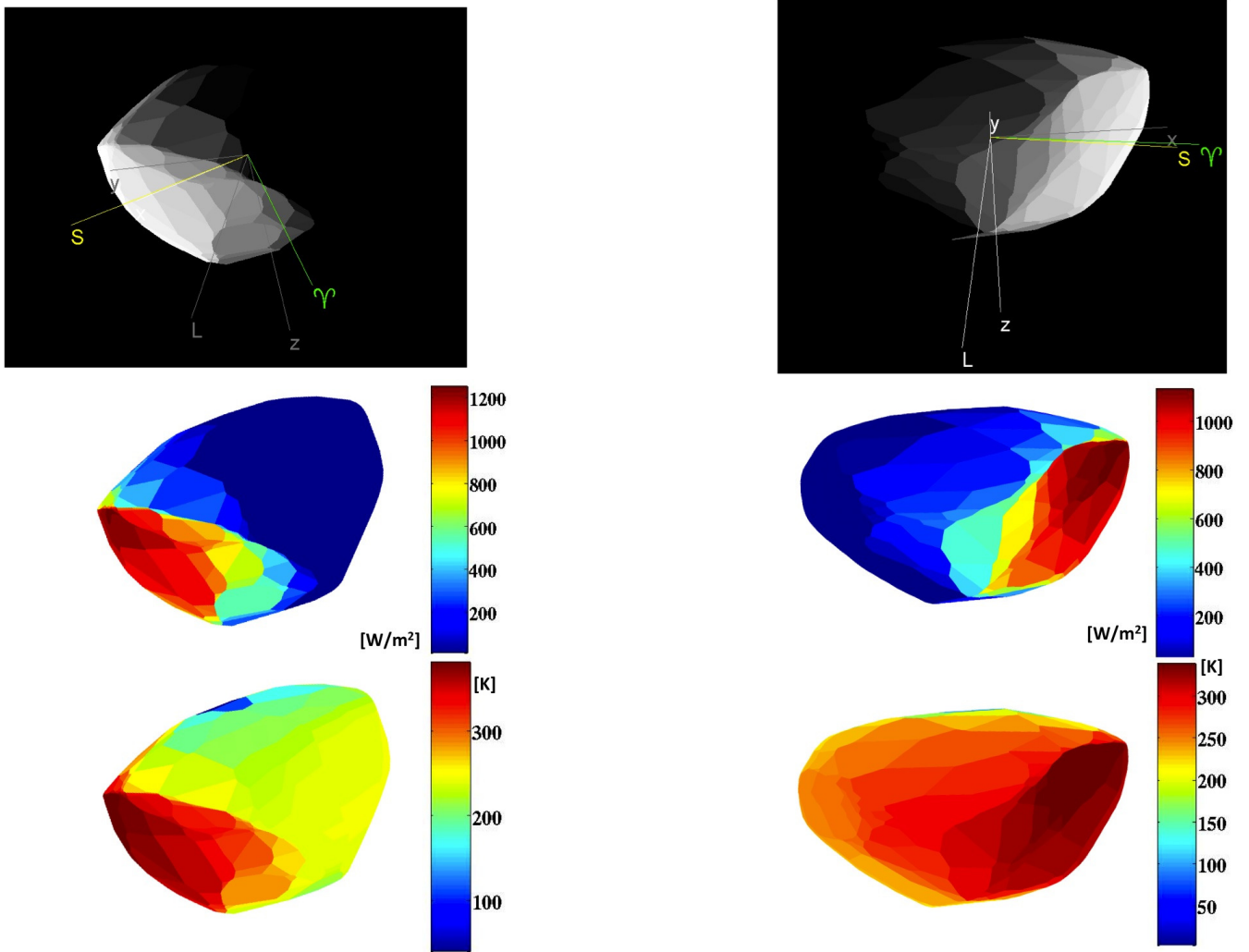
Fig. 3. Viewing geometry during the two Herschel observing epochs at phase angles of roughly 60° angle before (left) and after opposition (right). Top: calculated observing geometry on basis of the nominal solution in Pravec et al. (2014). L is fixed vector of angular momentum, the Aries sign is the X axis of the ecliptical frame, S is a direction to the Sun, and x, y, z are the axes of the asteroid co-rotating coordinate frame (corresponding to the smallest, intermediate and the largest moment of inertia of the body, respectively). Middle: The solar insolation in [W/m²]. Bottom: TPM temperature calculations assuming a Itokawa-like thermal inertia of $600 \, \mathrm{Jm^{-2}s^{-0.5}K^{-1}}$.
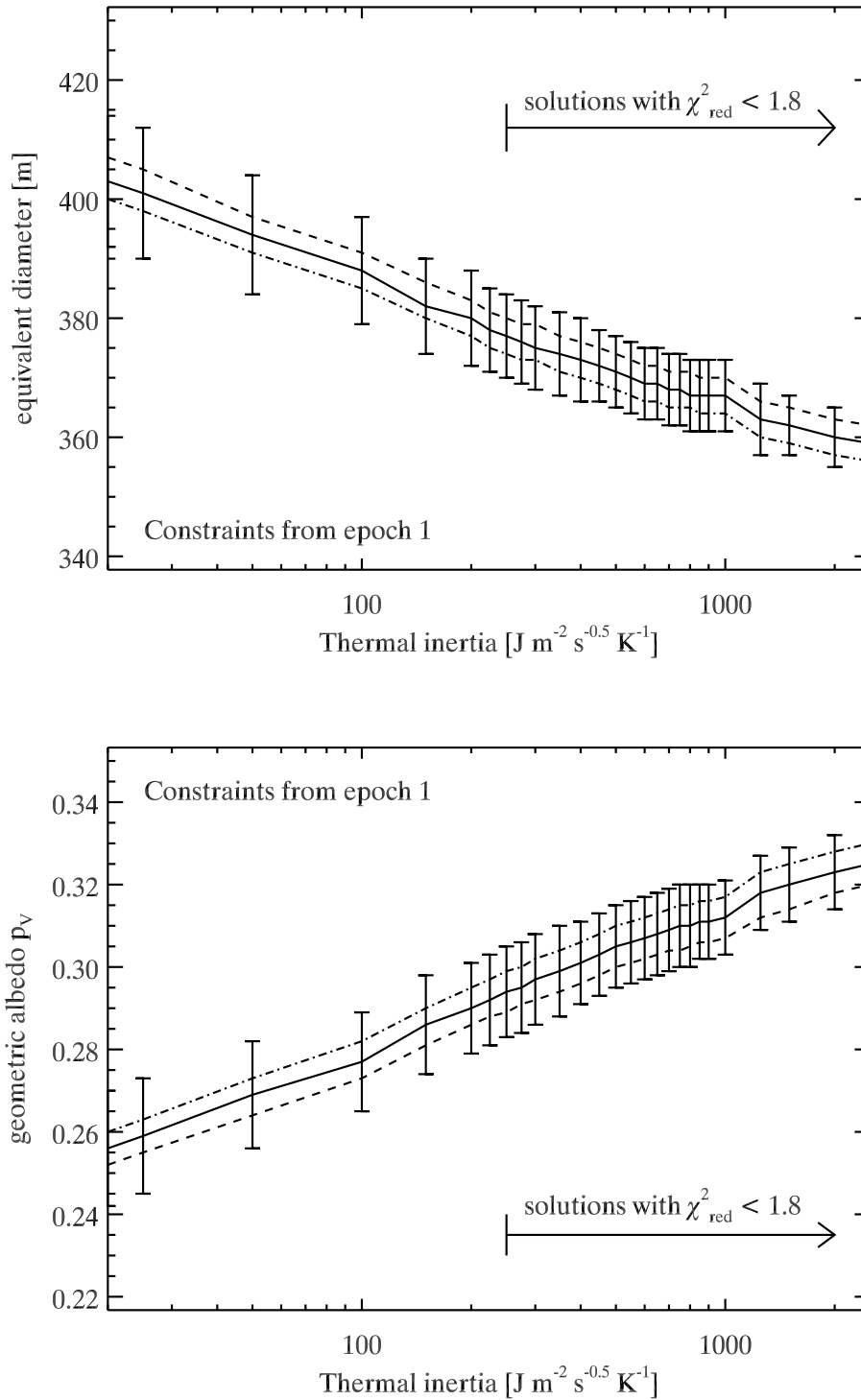
Fig. 4. The radiometrically derived size (top) and albedo (bottom) as a function of thermal inertia. The influence of model surface roughness is shown as dashed (low roughness) and dotted-dashed (high roughness) lines. The errorbars indicate the standard deviation of observation-to-model ratios for our epoch-1 measurements.
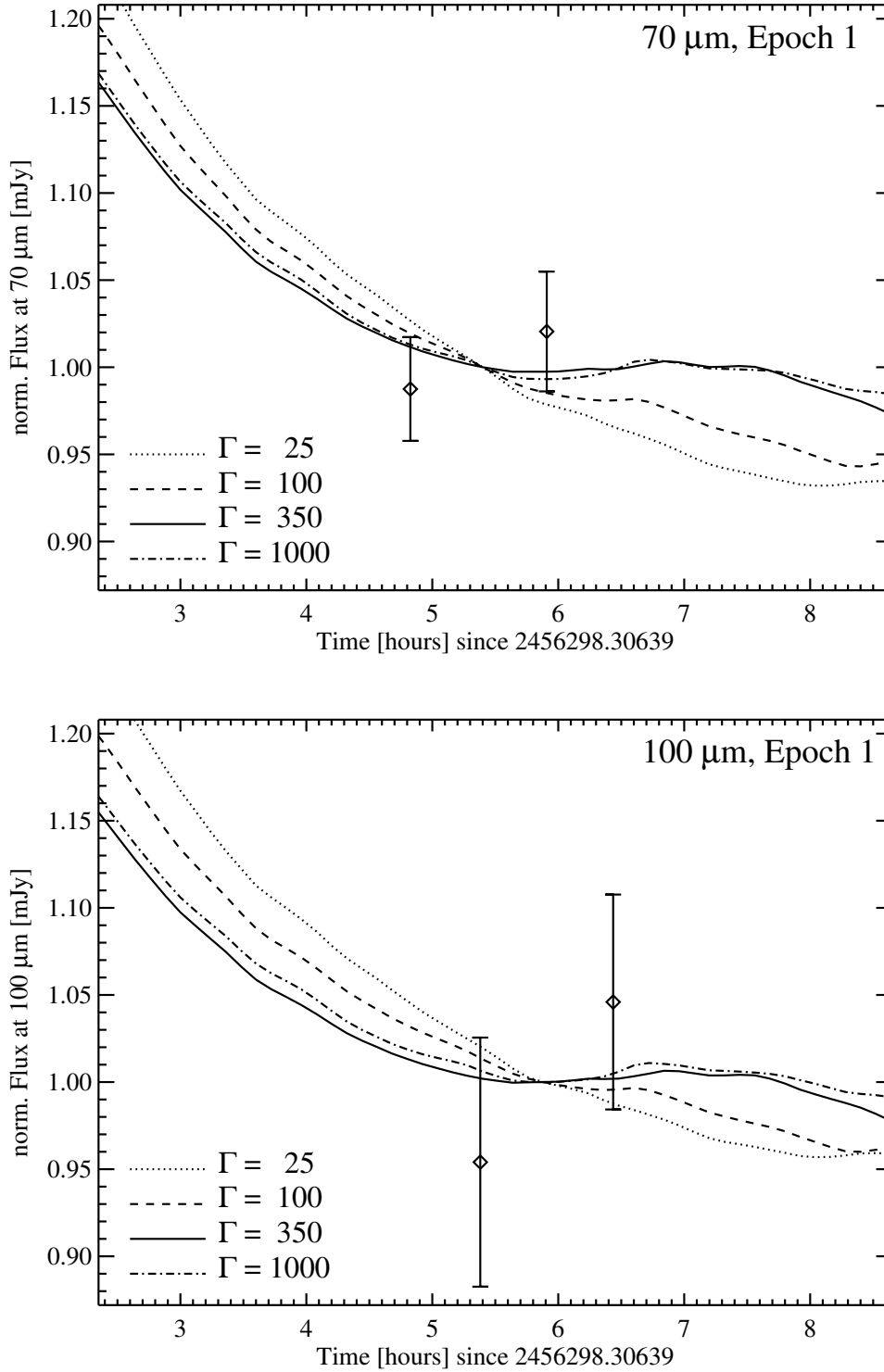
Fig. 5. The TPM lightcurves at $70\,\mu$m (top) and at $100\,\mu$m (bottom) together with the observed fluxes and their errorbars, all normalised at mid-time. The influence of thermal inertia on the lightcurve is clearly visible and the measurements seem to follow the higher-inertia curves.
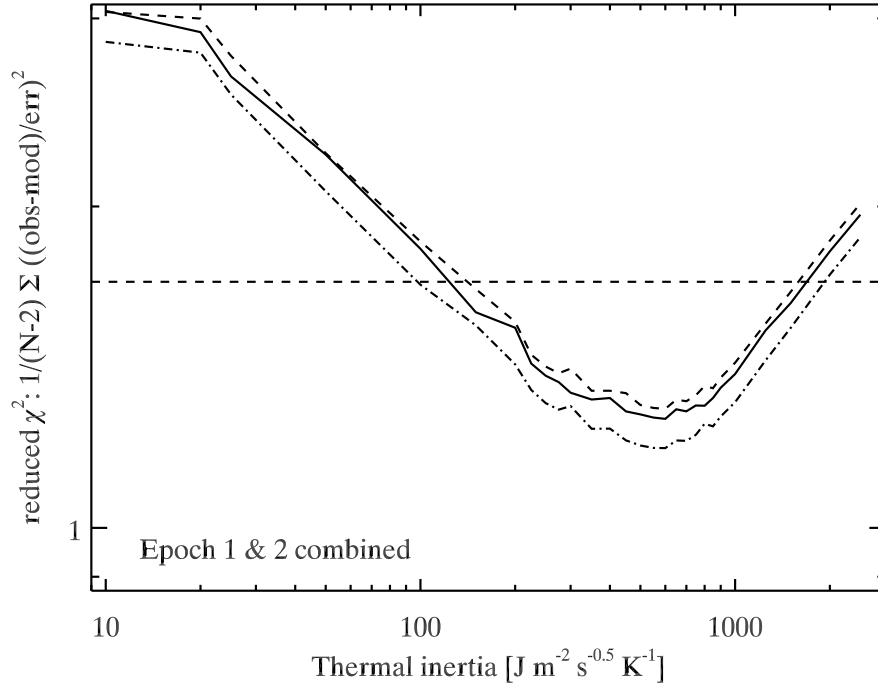
Fig. 6. Reduced χ^2-values calculated for the radiometric analysis of the combined epoch-1 and epoch-2 dataset. The dashed line shows the low roughness case, while the dashed-dotted line represents the very high roughness case. Good-fit solutions are found below the dashed horizontal line representing the reduced χ^2 threshold for five measurements at 1.7.
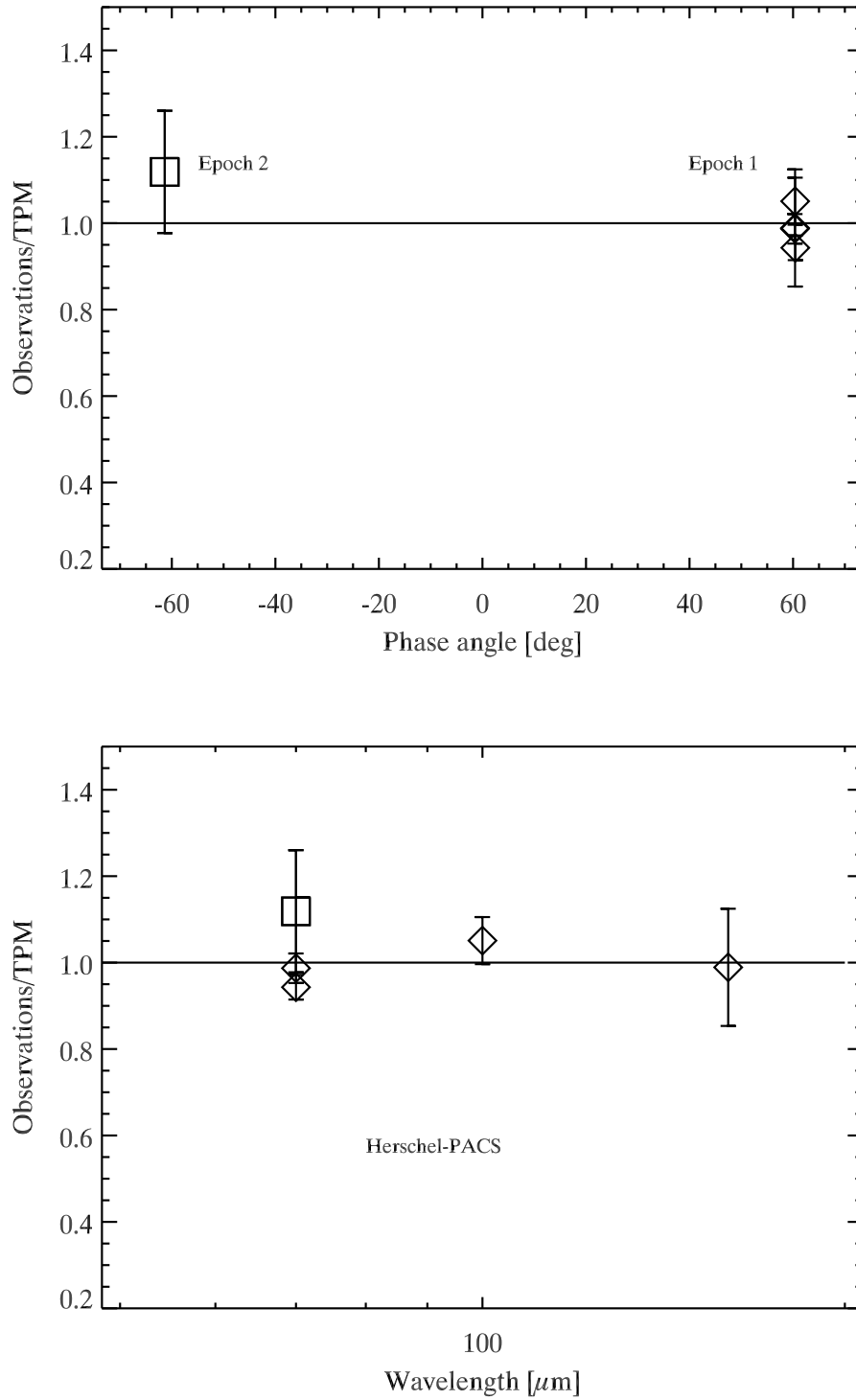
Fig. 7. The calibrated PACS observations divided by the best TPM solution as a function of phase angle (top) and as a function of wavelength (bottom).
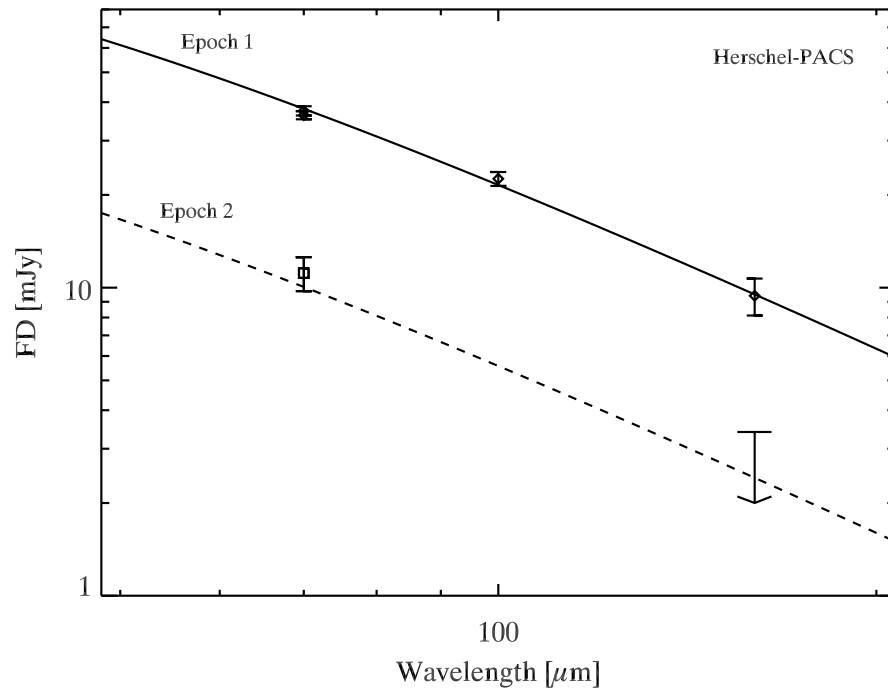
Fig. 8. The observed absolute fluxes and the corresponding TPM predictions. The best TPM solution is shown as solid line (epoch 1) and as dashed line (epoch 2).